



## Article

# Influence of Sulfate and Nitrate for Lanthanum (III) Adsorption on Bentonite: Implications for Rare Earth Wastewater Disposal

Zongke Zhou <sup>1</sup>, Quan Wan <sup>1,2</sup> , Wenbin Yu <sup>1</sup> , Xin Nie <sup>1</sup>, Shuguang Yang <sup>1</sup>, Shuqin Yang <sup>1</sup> and Zonghua Qin <sup>1,\*</sup>

<sup>1</sup> State Key Laboratory of Ore Deposit Geochemistry, Institute of Geochemistry, Chinese Academy of Sciences, Guiyang 550081, China; zhouzongke@mail.gyig.ac.cn (Z.Z.); wanquan@vip.gyig.ac.cn (Q.W.); yuwenbin@mail.gyig.ac.cn (W.Y.); niexin@mail.gyig.ac.cn (X.N.); yangshuguang@mail.gyig.ac.cn (S.Y.); yangshuqin@mail.gyig.ac.cn (S.Y.)

<sup>2</sup> CAS Center for Excellence in Comparative Planetology, Hefei 230026, China

\* Correspondence: qinzonghua@mail.gyig.ac.cn

**Abstract:** The direct discharge of rare earth wastewater causes the waste of resources and heavy metal pollution. This paper compared the adsorption behaviors of lanthanide ions on bentonite under sulfate and nitrate systems by examining the factors affecting the adsorption, such as adsorption time, pH, background electrolyte concentration, and initial rare earth ion concentration. It was shown that the sulfate system was more favorable for the adsorption of rare earth ions on the bentonite surface. The maximum adsorption capacity in the sulfate system was about 1.7 times that in the nitrate system. In contrast, the adsorption under the nitrate system was more sensitive to the changes in pH and background electrolyte concentration. The adsorption processes under both systems are spontaneous physical adsorption processes ( $\Delta G^\theta$  are from  $-27.64$  to  $-31.48$  kJ/mol), and both are endothermic ( $\Delta H^\theta$  are 10.38 kJ/mol for the nitrate and 7.53 kJ/mol for the sulfate) and entropy-increasing ( $\Delta S^\theta$  are 61.54 J/mol for the nitrate and 76.24 J·mol<sup>-1</sup> for the sulfate) processes. This study helps to provide information about the optimizing process parameters for the adsorption treatment of rare earth wastewater using bentonite.

**Keywords:** rare earth element; bentonite; sulfate; nitrate; adsorption; thermodynamics; kinetics



**Citation:** Zhou, Z.; Wan, Q.; Yu, W.; Nie, X.; Yang, S.; Yang, S.; Qin, Z. Influence of Sulfate and Nitrate for Lanthanum (III) Adsorption on Bentonite: Implications for Rare Earth Wastewater Disposal. *Minerals* **2024**, *14*, 268. <https://doi.org/10.3390/min14030268>

Academic Editor: Raúl Fernández

Received: 25 January 2024

Revised: 14 February 2024

Accepted: 19 February 2024

Published: 2 March 2024



**Copyright:** © 2024 by the authors. Licensee MDPI, Basel, Switzerland. This article is an open access article distributed under the terms and conditions of the Creative Commons Attribution (CC BY) license (<https://creativecommons.org/licenses/by/4.0/>).

## 1. Introduction

Rare earth elements include the 15 lanthanides with atomic numbers ranging from 57 to 71, as well as scandium and yttrium. Due to their unique and diverse electronic properties [1], rare earth elements have various applications in many industrial and high-tech fields, such as metallurgy [2], catalysis [3], ceramics [4], permanent magnet materials [5], superconducting materials [6], and weapons [7]. Many countries recognize them as critical metallic elements with strategic significance [8].

The ores mainly used to produce rare earth elements include independent rare earth minerals (e.g., monazite, bastnasite, and xenotime) and ion-adsorbed rare earth minerals [9]. In addition, deep-sea sediments, phosphorites, bauxites, and tailings (e.g., red mud and phosphogypsum) are potential sources for rare earth extraction [10]. Regardless of the type of ores used as raw materials, large quantities of wastewater containing specific concentrations of rare earth elements are generated during production processes such as mining, beneficiation, separation, smelting, and processing [11,12]; e.g., mine drainage from the Wisniowka mine in Poland contained 24,800 µg/L of rare earth ions [13]. The direct discharge of the wastewater containing rare earth cations will result in the waste of resources and the formation of heavy metal pollution.

Numerous conventional techniques (e.g., precipitation [14], flotation [15], and coagulation/flocculation [16,17]) and new methods (e.g., ultrafiltration/nanofiltration [18–20], biosorption [21], electrodialysis [22], and photocatalysis [23]) are used for the removal of heavy metals from wastewater. Like other heavy metal pollution treatment methods, rare

earth elements can be treated and recovered from wastewater by chemical, physicochemical, and biological methods [24–26]. However, adsorption is widely used in treating heavy metals in wastewater, which also contains rare earth ions, as a method that combines many advantages, such as being cost-effective, selective, and effective in separating pollutants at low concentrations [27–31].

There are many types of adsorbents used for the adsorption treatment of heavy metals in wastewater, e.g., activated carbon [32], zeolite [33], resin [34], biomass [35,36], clay mineral [37], and inorganic–organic composites [38]. Bentonite is a natural adsorbent with a high adsorption capacity and a low price. Bentonite is composed primarily of the clay mineral montmorillonite, which comprises two silicon–oxygen tetrahedral sheets sandwiched with an aluminum–oxygen octahedral sheet to form a 2:1 type layer. These layers are stacked to form the basic layered structure of montmorillonite. The layers are negatively charged because there are often isomorphic substitutions in montmorillonite layers (e.g.,  $\text{Mg}^{2+}$  replaces  $\text{Al}^{3+}$  in octahedral sheets, and  $\text{Al}^{3+}$  replaces  $\text{Si}^{4+}$  in tetrahedral sheets). There are hydrated cations, such as calcium or sodium, between the layers, which balance the negative charges of the layer [39,40]. This structure endows montmorillonite with a good swelling and ion exchange capacity, resulting in an excellent adsorption and removal efficiency of many cationic pollutants, including heavy metals [41–44].

Some researchers have discussed the influencing factors and adsorption mechanism of removing or recovering rare earth elements using bentonite. Coppin et al. analyzed the adsorption of a mixed solution containing 14 rare earth elements on montmorillonite and kaolinite. They found that ionic strength is a vital adsorption factor in addition to the surface properties of clay minerals and pH. Especially under high ionic strength, a fractionation of light and heavy rare earth elements occurs [45]. Alshameri et al. compared the adsorption behavior of four clay minerals, including montmorillonite, for the light rare earth element lanthanum and the heavy rare earth element ytterbium, as well as the differences in leaching behavior after adsorption. Notably, they found that ammonium ions would cause an increased pH and reduce the ion-exchanged rare earth elements [46]. At the same time, other researchers hope to improve the adsorption efficiency of rare earth elements in wastewater by modifying bentonite. Fang et al. investigated the factors affecting the adsorption of rare earth elements by sulfuric acid-modified montmorillonite, as well as the kinetics and thermodynamics of the adsorption process [47]. Wang discussed the adsorption behavior of five rare earth ions on montmorillonite loaded with zero-valent iron nanoparticles and found that the adsorption mechanism is the combination of ion exchange and surface complexation [48].

In addition, rare earth wastewater usually contains a large amount of sulfate, which comes from three primary sources. (1) The acid-leaching process of rare earth minerals may use a large amount of sulfuric acid [49]. (2) The leaching process of ion-adsorbed rare earth deposits uses a large amount of sulfate as a leaching agent [50]. (3) The pyrite associated with rare earth ores [51,52] is easily oxidized to generate sulfate during mining and processing. Many studies have found that sulfate has a significant impact on the adsorption process of heavy metals. For example, Cheira explored the adsorption performance of Th(IV) on poly(sulfonamide)/nano-silica composites in sulfate solution, and the adsorption process conformed to the pseudo-second-order kinetic model and the Langmuir adsorption isotherm model [53]. Liu et al. investigated the effect of sulfate on the adsorption/desorption behavior of copper ions on the ferrihydrite surface. They found that sulfate contributes to the adsorption of copper ions and controls copper speciation [54]. Gu et al. analyzed the effect of sulfate on the adsorption, desorption, and fractionation of rare earth elements on the surfaces of kaolinite and ferrihydrite. They found that sulfate had a negligible effect on the adsorption and fractionation of rare earth elements on the surface of kaolinite. However, it contributed to rare earth desorption from the kaolinite surface [55]. However, there needs to be more systematic research on the effect of sulfate on the adsorption of rare earth cations by bentonite.

This paper used lanthanum as a surrogate of rare earth elements to compare the differences in the adsorption behavior of lanthanum by bentonite with sulfate and nitrate. By examining the effects of time, pH, background electrolyte concentration, and initial rare earth ion concentration on the adsorption process, and combining adsorption kinetic and thermodynamic model fitting analysis, we speculated on the different adsorption mechanisms of lanthanum cations by bentonite in nitrate and sulfate systems. This study provides information about the parameter optimization of the adsorption process by bentonite for rare earth wastewater treatment.

## 2. Materials and Methods

### 2.1. Minerals and Reagents

The bentonite sample came from Inner Mongolia, China. The sample was washed, crushed, ground, gravity-settled, and dried at 50 °C for characterization and subsequent experiments. The sample's cation exchange capacity (CEC) was 90.3 mmol/100 g using the ammonium exchange method [56].

Lanthanum nitrate ( $\text{La}(\text{NO}_3)_3$ ) and azoarsine III ( $(\text{HO})_2\text{C}_{10}\text{H}_2(\text{SO}_3\text{H})_2(\text{N}=\text{NC}_6\text{H}_4\text{AsO}_3\text{H}_2)_2$ ) were purchased from Shanghai Aladdin Biochemical Technology Co., Ltd. (Shanghai, China). Both were AR reagents and were used as received without further purification.

### 2.2. Characterization of Bentonite Sample

#### 2.2.1. Phase

The sample phases were measured using an X-ray powder diffractometer (Empyrean, PANalytical, Almelo, The Netherlands). The sample was ground to about 40  $\mu\text{m}$  and then placed on the sample holder for testing. The test was performed using  $\text{Cu-K}\alpha$  ( $\lambda = 0.154 \text{ nm}$ ) radiation at a tube voltage of 40 kV and a tube current of 40 mA. The scanning range was 4–70° (2 $\theta$ ); the detector was PIXcel3D (PANalytical, Almelo, The Netherlands), the scanning speed was 0.22° per second, and the total scanning time was 5 min.

#### 2.2.2. Thermal Analysis

Thermogravimetric analysis was performed on a simultaneous thermal analyzer (STA 449 F3 Jupiter, Netzsch, Selb, Germany). Approximately 10 mg of the sample was added to an alumina crucible. The mass loss was determined at 40–1200 °C under a purge of high-purity argon (99.999%) at a gas flow rate of 60 mL/min, and a protective argon gas (99.999%) at a gas flow rate of 20 mL/min, with a ramp rate of 10 °C/min.

#### 2.2.3. Chemical Composition

The major elements of the sample were dried at 80 °C, prepared using the fusion bead method, and tested on an X-ray fluorescence spectrometer (X-RARL Perform' X 4200, Thermo Scientific, Waltham, MA, USA). The sample, ball-milled to less than 75  $\mu\text{m}$ , was mixed with flux and release agent and then melted at 1200 °C for 10 min to prepare a glass disc for a test. The X-ray tube voltage was 50 kV, and the current was 50 mA. The relative standard deviation of the repeatability was better than 0.1%.

#### 2.2.4. Morphology

A scanning electron microscope (Scios, FEI, Sunnyvale, OR, USA) observed the sample's morphology. The ethanol suspension of the mineral powder was dropped onto the single-crystal silicon wafer and then air-dried. The test was conducted after spraying with a carbon film. The test acceleration voltage was 2 kV.

#### 2.2.5. Particle Size

A particle size analysis of the samples was performed on a laser particle size analyzer (Omni, Brookhaven Instruments, New York, NY, USA). A total of 0.01 g of sample was dispersed in 20 mL of deionized water to make a suspension, which was poured into a

square polystyrene cell and tested at 659 nm. The scattering angle was  $90^\circ$ , the count rate was 522.5 kcps, and the equilibration time was 30 s.

#### 2.2.6. Specific Surface Area and Pore Structure

The specific surface area and pore structure of the sample were measured on an automatic specific surface area and porosity analyzer (Autosorb-iQ<sup>2</sup>, Quantachrome, Gainesville, FL, USA) at 77 K. Before testing, about 100 mg of bentonite powder was added into the sample tube and vacuum-degassed at 250 °C for 6 h. The specific surface area was calculated using the multi-point Brunauer–Emmett–Teller (BET) method based on the data between the relative pressure  $P/P_0 = 0.05 - 0.35$  [57]. The total pore volume and pore distribution were fitted using the nonlocal density functional theory (NLDFT) model for slit pores based on the data between the relative pressure  $P/P_0 = 10^{-7} - 1$  [58].

#### 2.2.7. Point of Zero Charge

The sample's point of zero charge was measured using an automatic potentiometric titrator (T50, Mettler Toledo, Columbus, OH, USA) equipped with a glass electrode (DGill-SC, Mettler Toledo). A total of 120 mL of deionized solution was added to a 250 mL Erlenmeyer flask containing 60 mg of bentonite powder. Then, the suspension was shaken at 200 revolutions per minute (rpm) and 25 °C in a thermostat shaker for 24 h. After preparing the suspension similarly, a supernatant was obtained by filtering the suspension using a polyethersulfone (PES) membrane with a pore size of 0.45 µm. A total of 100 mL of suspension or supernatant was dispensed to a titration cup, and the liquid was ventilated with argon gas until the pH remained unchanged. A total of 0.1 mol/L HNO<sub>3</sub> solution was used to adjust the pH of the liquid to below 3. After the pH value was stable, 0.1 mol/L NaOH was slowly titrated into the liquid until pH = 11. The intersection of the suspension and supernatant titration curves was the sample's point of zero charge.

#### 2.2.8. ζ Potential

The ζ potential of the sample was measured using a zeta potential analyzer (Omni, Brookhaven Instruments, New York, NY, USA). A total of 100 mL of 0.05 mol/L Na<sub>2</sub>SO<sub>4</sub> (or NaNO<sub>3</sub>) solution was added into a beaker containing 50 mg of sample to prepare a suspension. The suspension was divided into five aliquots, and 0.1 mol/L H<sub>2</sub>SO<sub>4</sub> (or HNO<sub>3</sub>) and NaOH solution were used to adjust the pH of the suspensions to the specified pH. A small amount of suspension of each pH was taken into a polystyrene cuvette for three consecutive tests.

#### 2.2.9. Infrared Spectroscopy

The infrared spectra of the samples before and after adsorption were measured using a Fourier transform infrared (FTIR) spectrometer (Vertex 70, Bruker, Ettlingen, Germany), equipped with an attenuated total reflection accessory (GladiATR, PIKE Technologies, Madison, WI, USA), scanning in a range of 400–4000 cm<sup>−1</sup> at a resolution of 1 cm<sup>−1</sup>.

### 2.3. Adsorption Experiment

A specific concentration of lanthanum nitrate and sodium sulfate (or sodium nitrate) solution was poured into a 50 mL stoppered Erlenmeyer flask containing bentonite powder, with a solid–liquid ratio of 0.01 g/20 mL. The suspension was adjusted to the specified pH value using different concentrations of NaOH and H<sub>2</sub>SO<sub>4</sub> (or HNO<sub>3</sub>). After sealing the Erlenmeyer flask, it was placed in a shaker and operated at 200 rpm and a specific temperature for a predetermined time, and then the suspension was filtered through a PES membrane with a pore size of 0.45 µm. The concentration of rare earth ions in the filtrate was measured using quartz cuvettes with azoarsena III spectrophotometry [59,60], and calculated according to the absorbance at 652 nm with an ultra-violet visible (UV-vis) spectrophotometer (Carry 300, Agilent Technologies, Santa Clara, CA, USA).

The adsorption efficiency ( $A_t$ , %) of bentonite for lanthanum cations is calculated according to Equation (1):

$$A_t = \frac{C_0 - C_t}{C_0} \times 100\% \quad (1)$$

where  $C_0$  is the initial concentration of the rare earth element (mol/L), and  $C_t$  is the rare earth element concentration (mol/L) in the supernatant when the adsorption time is  $t$  [46].

The adsorption capacity ( $Q_t$ , mg/g) of bentonite for lanthanum cations was calculated according to Equation (2):

$$Q_t = \frac{VM(C_0 - C_t)}{m} \quad (2)$$

where  $V$  is the volume of the suspension (mL),  $M$  is the molar mass of lanthanum (138.9 g/mol),  $m$  is the mass of bentonite (g), and  $C_0$  and  $C_t$  are as mentioned above [46].

The adsorption kinetics was fitted using pseudo-first-order kinetics and pseudo-second-order kinetics models, and the nonlinear forms of the models are shown in Equations (3) and (4), respectively.

$$Q_t = Q_e \left(1 - e^{-k_1 t}\right) \quad (3)$$

$$Q_t = \frac{k_2 Q_e^2 t}{1 + k_2 Q_e t} \quad (4)$$

where  $Q_t$  and  $Q_e$  are the adsorption capacities of  $\text{La}^{3+}$  at time  $t$  and equilibrium (mg/g), respectively.  $k_1$  (1/h) and  $k_2$  (g/(mg·min)) are the adsorption rate constants of pseudo-first-order kinetics and pseudo-second-order kinetics, respectively [61].

The adsorption isotherm was fitted using the Langmuir and Freundlich models.

The Langmuir model describes single-layer adsorption on a uniform surface, and its linear expression is:

$$\frac{C_e}{Q_e} = \frac{1}{K_L Q_{max}} + \frac{C_e}{Q_{max}} \quad (5)$$

where  $K_L$  is the Langmuir constant (L/mg),  $C_e$  is the equilibrium concentration of  $\text{La}^{3+}$  (mg/L), and  $Q_e$  and  $Q_{max}$  are the equilibrium and maximum adsorption capacity (mg/g), respectively [62].

The Freundlich adsorption isotherm is an empirical formula summarized based on a large amount of experimental data. It is suitable for multi-molecular layer physical adsorption on non-uniform surfaces. Its linear expression is:

$$\lg Q_e = \lg K_F + \frac{1}{n} \lg C_e \quad (6)$$

where  $Q_e$  is the equilibrium adsorption capacity (mg/g),  $K_F$  is the Freundlich adsorption coefficient,  $n$  is a constant, and  $C_e$  is the equilibrium concentration of  $\text{La}^{3+}$  (mg/g) [62].

The thermodynamic parameters of the adsorption process, such as the standard Gibbs free energy ( $\Delta G^\theta$ , kJ/mol), are calculated based on the isotherm model parameters:

$$\Delta G^\theta = -RT \ln K \quad (7)$$

where  $R$  is the gas constant (8.314 J/(mol K)),  $T$  is the thermodynamic temperature (K), and  $K$  is a constant (like  $K_L$  in the Langmuir equation) [63].

The standard enthalpy change ( $\Delta H^\theta$ , kJ/mol) and standard entropy change ( $\Delta S^\theta$ , kJ/mol) of the adsorption process are calculated by fitting according to Equation (8):

$$\Delta G^\theta = \Delta H^\theta - T \Delta S^\theta \quad (8)$$

where  $\Delta G^\theta$  is the standard Gibbs free energy (kJ/mol), and  $T$  is the thermodynamic temperature (K) [63].

### 3. Results and Discussion

#### 3.1. Characterization of Bentonite Sample

##### 3.1.1. Phase

Figure 1 shows the X-ray diffraction pattern of the sample. According to the ICDD's powder diffraction file (PDF), the sample possesses typical diffraction peaks of montmorillonite, and the prominent characteristic peaks are solid and sharp, indicating that montmorillonite has good crystallinity. The (001) crystal plane spacing of the sample is 1.58 nm, which may be calcium montmorillonite.

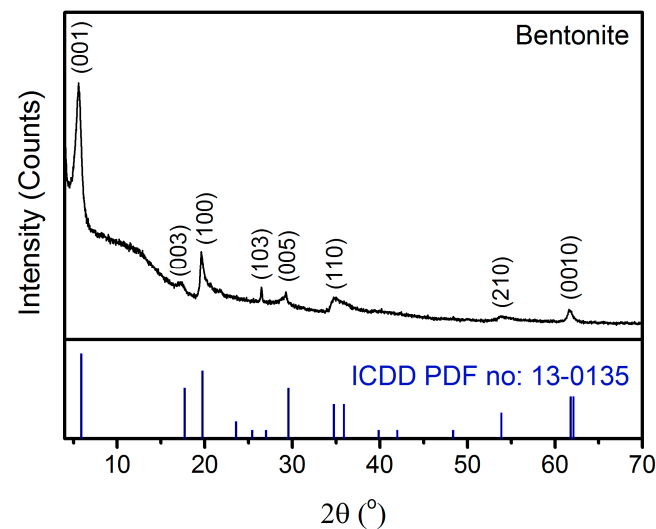


**Figure 1.** XRD pattern of the bentonite sample and the ICDD powder diffraction file (PDF) of montmorillonite.

##### 3.1.2. Thermal Analysis

Based on the first-order differential curve of the thermogravimetric curve (DTG) of the sample, the mass loss of this bentonite sample can be categorized into two stages [64] (Figure 2): the dehydration process occurs from 40 to 300 °C, and the sample's water content is about 10.2%. The temperatures at which the maximum rates of adsorbed and interlayer water loss occur are 106 °C and 146 °C, respectively. The mass loss after 300 °C is mainly due to dehydroxylation, with a mass loss of −4.8%, and the temperature at which the maximum dehydroxylation rate occurs is 619 °C.

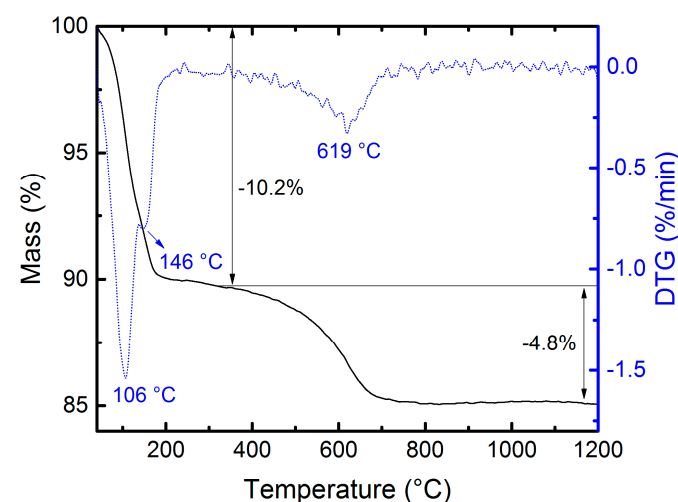


**Figure 2.** Thermogravimetric curve and its first-order differential curve (DTG) of the bentonite sample.

### 3.1.3. Chemical Composition

According to the major element composition of the sample in Table 1, it can be seen that the sample mainly contains silicon and aluminum, which are the central elements of the silicon–oxygen tetrahedral and the aluminum–oxygen octahedral sheets, respectively. Since isomorphic substitutions often occur in the octahedral sheets of montmorillonite, elements such as iron and magnesium are likely to exist in the octahedral sheets. Calcium mainly exists between layers, and its content is significantly higher than sodium and potassium, indicating that the sample mainly contains calcium montmorillonite, consistent with the XRD results. Based on the major element content, the mineral chemical formula of the montmorillonite can be calculated as:  $(\text{Ca}_{0.24}\text{K}_{0.01})[(\text{Al}_{1.23}\text{Mg}_{0.49}\text{Fe}_{0.24})(\text{Si}_{3.97}\text{Al}_{0.03})\text{O}_{10}(\text{OH})_2]\cdot n\text{H}_2\text{O}$ .

**Table 1.** Major element contents of the bentonite sample (wt.%).

SiO <sub>2</sub>	Al <sub>2</sub> O <sub>3</sub>	Fe <sub>2</sub> O <sub>3</sub>	MgO	CaO	Na <sub>2</sub> O	K <sub>2</sub> O	MnO	P <sub>2</sub> O <sub>5</sub>	TiO <sub>2</sub>	L.O.I. *	Total
59.99	16.13	4.85	5.00	3.43	0.40	0.16	0.022	0.046	0.283	9.92	100.23

\* L.O.I.: Loss on ignition.

### 3.1.4. Morphology

It can be seen from the scanning electron microscope image of the sample (Figure 3) that the particle size of the sample is approximately a few microns. The sample has a lamellar structure, and the lamellae are irregularly stacked to form cotton-like aggregates.

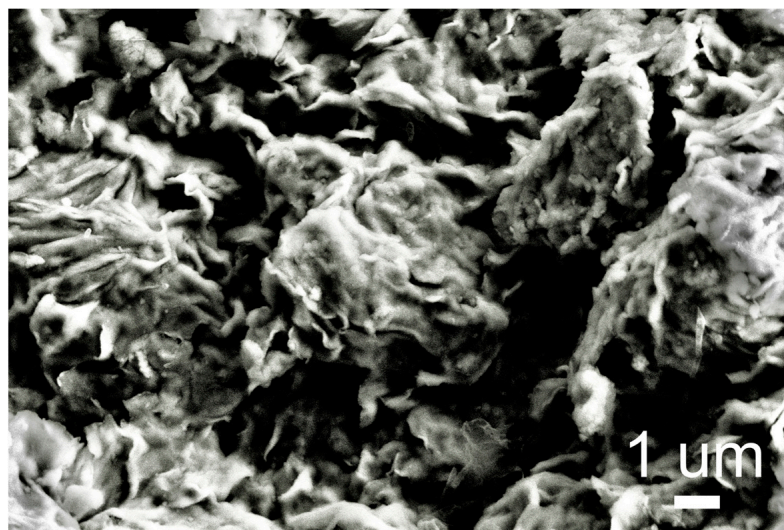


**Figure 3.** Scanning electron microscope image of the bentonite sample.

### 3.1.5. Particle Size

The particle size distribution of the sample obtained from the cumulative scattering intensity curves (Figure 4) shows that the particle sizes were mainly concentrated in 3–4 μm and 7–8 μm. This may be due to the surface charges of the bentonite [39], resulting in the agglomeration of a portion of the crushed particles after they are dispersed in the aqueous solution during testing.

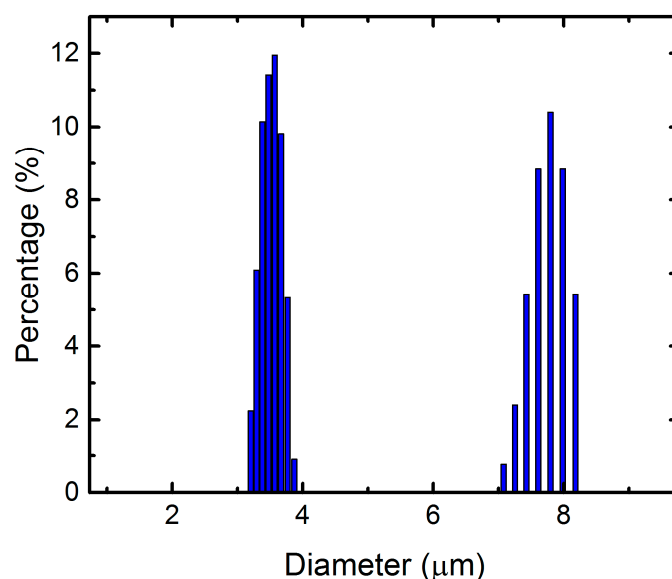


**Figure 4.** Particle size distribution of the bentonite sample.

### 3.1.6. Specific Surface Area and Pore Structure

The nitrogen adsorption–desorption isotherm of the sample (Figure 5) rises rapidly under low relative pressure, and the curve is convex. There is no adsorption saturation under high relative pressure and an obvious adsorption hysteresis loop. According to the IUPAC classification standard [65], this sample has a type IV adsorption isotherm. The hysteresis loop is caused by capillary condensation, which essentially results from the mesoporous structure in the sample. The hysteresis loop of the adsorption–desorption curve of this sample belongs to the H3 type, indicating that the pore has a flat slit structure, which is consistent with the layer structure of montmorillonite. The BET specific surface area of the sample is  $83 \text{ m}^2/\text{g}$  (the correlation coefficient is 0.999990, and the C constant is 255.673).

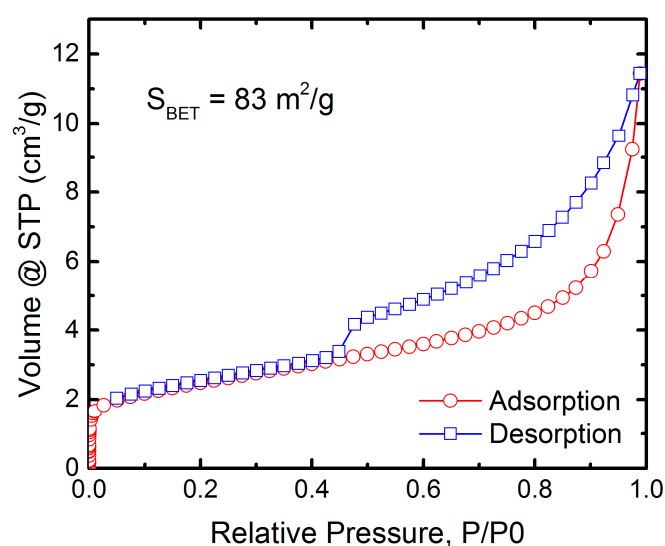


**Figure 5.** Nitrogen adsorption–desorption isotherm of the bentonite sample.

From the total pore volume and pore size distribution diagram of the sample obtained using the NLDFT method (Figure 6), it can be seen that the total pore volume of the bentonite sample is  $0.143 \text{ cm}^3/\text{g}$ , and the average pore diameter of the sample is  $3.8 \text{ nm}$  (the fitting error is 2.141%).

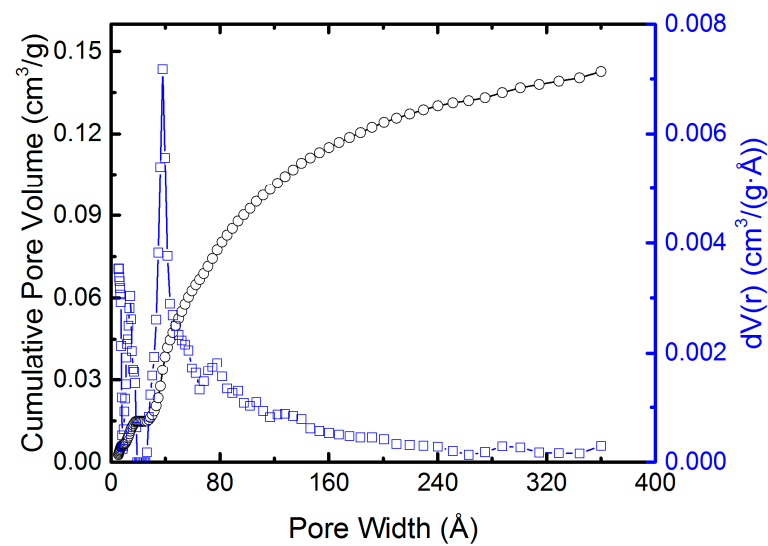


**Figure 6.** Total pore volume and pore size distribution of the bentonite sample.

### 3.1.7. Point of Zero Charge

Montmorillonite has two types of surfaces. The basal surface usually has a permanent negative charge due to isomorphous substitution; the edge surface has a variable charge due to the protonation or deprotonation of hydroxyl groups with the changes in pH [66]. It is usually impossible to measure the zero charge point of such clay minerals with both permanent charge and variable charge through acid-base titration at different ionic strengths [67]. Therefore, a method of titrating the sample suspension and the mineral-free supernatant separately was adopted to obtain the sample's point of zero charge.

According to the intersection of the potentiometric titration curves of the bentonite suspension and the corresponding supernatant (Figure 7), it can be seen that the apparent point of zero charge on the edge surface of the montmorillonite is 9.5. When  $\text{pH} < 9.5$ , the edge surface of montmorillonite is positively charged; when  $\text{pH} > 9.5$ , the edge surface is negatively charged.

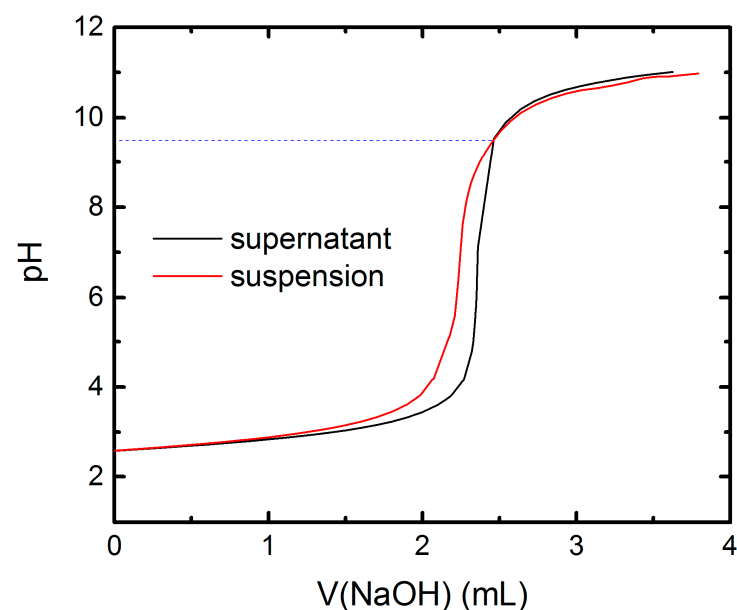


**Figure 7.** Potentiometric titration curves of the bentonite suspension and the corresponding supernatant.

### 3.1.8. $\zeta$ Potential

The difference in the sample's  $\zeta$  potential under the sodium nitrate and sodium sulfate systems (Figure 8) is slight, ranging from  $-30$  to  $-10$  mV. Generally, the  $\zeta$  potential value of highly dispersed particles is more significant than  $+30$  mV or less than  $-30$  mV [68]. The absolute value of the sample's  $\zeta$  potential is less than 30 mV, indicating that the repulsion between bentonite particles is weak, the stability of the suspension is poor, and it is easy to aggregate and settle. The poor suspension stability of the system is also responsible for the fluctuations in the measured data, and it is beneficial to solid–liquid separation and adsorbent recovery after adsorption.

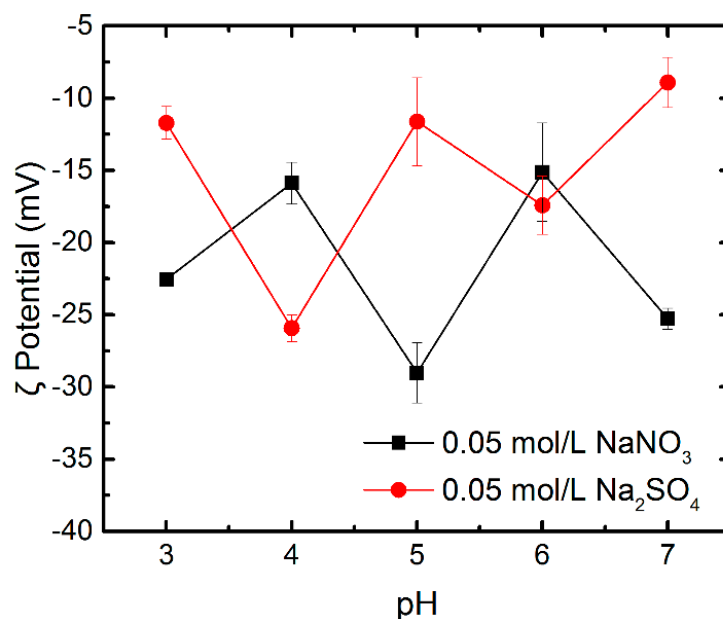


**Figure 8.**  $\zeta$  potentials of the bentonite sample under different pH and background electrolytes.

### 3.1.9. Infrared Spectroscopy

The FTIR spectra of the sample before and after adsorption in nitrate and sulfate are given in Figure 9, and the assignments of the adsorption peaks [69,70] are listed in Table 2. It can be seen that no new absorption peaks or significant shifts of absorption peaks are found. This may be because the lanthanide ions do not form stable chemical bonds with the surface adsorption sites, thus having less effect on the functional group vibration of the pristine bentonite [55].

**Table 2.** Positions and assignments of the FTIR vibration bands.

Position (cm <sup>-1</sup> )	Assignment
3614	–OH stretching of Al–OH and Mg–OH
3391	–OH stretching of interlayer water
1630	–OH deformation of interlayer water
991	Si–O stretching
914	–OH deformation of Al–OH
837	In-plane bending of CO <sub>3</sub> <sup>2–</sup>
796	–OH deformation of Mg–OH
511	Deformation of Si–O–Al
422	Deformation of Si–O–Si

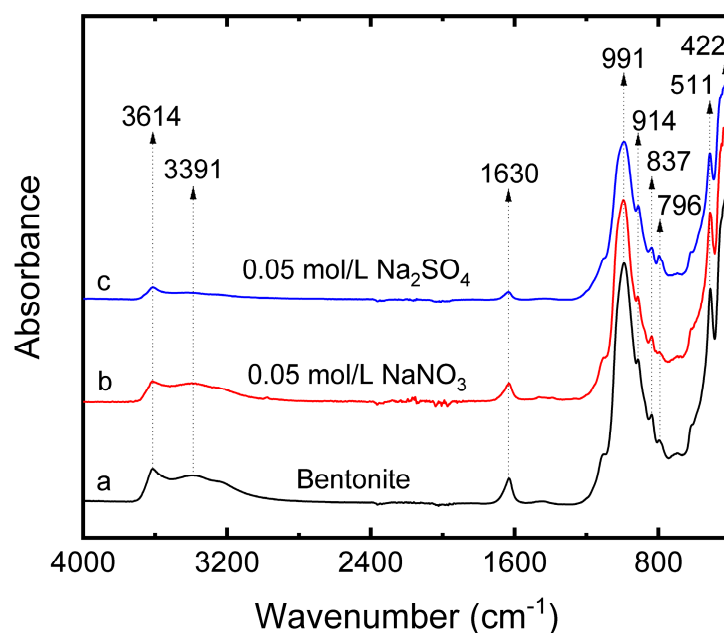


**Figure 9.** FTIR spectra of the sample before and after the adsorption of lanthanum. a. Pristine bentonite. b. Product after adsorption in 0.05 mol/L  $\text{NaNO}_3$ . c. Product after adsorption in 0.05 mol/L  $\text{Na}_2\text{SO}_4$ . (Initial  $\text{La}^{3+}$  concentration is 500  $\mu\text{mol/L}$ . pH is 6. Temperature is 25  $^\circ\text{C}$ . Time is 24 h).

### 3.2. Reliability of Concentration Determination Method

This concentration determination method utilizes the formation of a complex of rare earth with arsenazo (III) under acidic conditions (pH approximately 3–4) [59], which exhibits a maximum absorption peak at a wavelength of 652 nm. Therefore, a linear relationship can be established between the different concentrations of rare earth ions and the corresponding absorbances at a wavelength of 652 nm. Then, the concentration of an unknown rare earth solution can be calculated by measuring its absorbance.

From the UV-vis spectra (Figure 10) and the standard curves (Figure 11) for the lanthanum concentration determination of solutions containing different background electrolytes (water, 0.05 mol/L  $\text{NaNO}_3$ , and 0.05 mol/L  $\text{Na}_2\text{SO}_4$ ), it can be seen that the absorbances of the aqueous solution system and the nitrate system are similar. In contrast, the absorbance of the sulfate system is smaller than those of the other two systems, but the maximum absorption peak of the complex does not shift. At the same time, the standard curves under all three systems have good linearity and repeatability. Therefore, this method possesses good reliability in determining the concentration of lanthanum ions in this article.

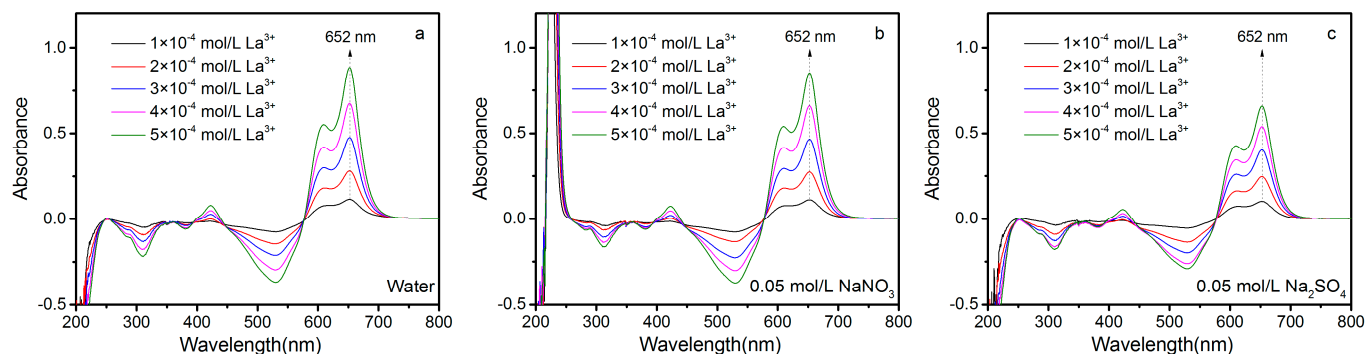


**Figure 10.** UV-vis spectra of lanthanum–arsenazo (III) complex solutions containing different background electrolytes ((a) water; (b) 0.05 mol/L  $\text{NaNO}_3$ ; (c) 0.05 mol/L  $\text{Na}_2\text{SO}_4$ ).

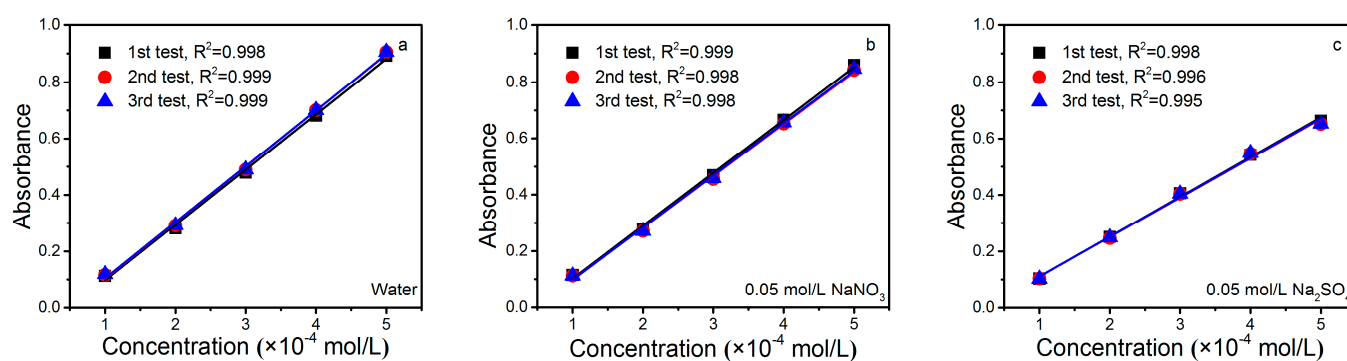


**Figure 11.** Standard curves for determining lanthanum concentration in different background electrolytes ((a) water; (b) 0.05 mol/L  $\text{NaNO}_3$ ; (c) 0.05 mol/L  $\text{Na}_2\text{SO}_4$ ).

### 3.3. Adsorption Equilibrium Time and Kinetics

It can be seen from the graph of the change in adsorption efficiency with time (Figure 12) that whether in a sodium nitrate system or a sodium sulfate system, the adsorption of lanthanum ions by bentonite first increased rapidly in a short time. At 30 min, the adsorption efficiencies under the sodium nitrate and sodium sulfate systems were 33% and 63%, respectively. Then, the adsorption efficiencies slowly increased until they reached adsorption equilibrium at about 24 h. At this time, the nitrate and sulfate systems' adsorption efficiencies were 41% and 68%, respectively, and the corresponding adsorption capacities were 57 mg/g and 94 mg/g, respectively. This is consistent with the adsorption behavior of trivalent ions (e.g.,  $\text{Cr}^{3+}$  [71]) on bentonite, where the entire adsorption process is divided into two stages: rapid adsorption and slow equilibration. The adsorption capacity of lanthanum by bentonite in the sulfate system is higher than that in the nitrate system.

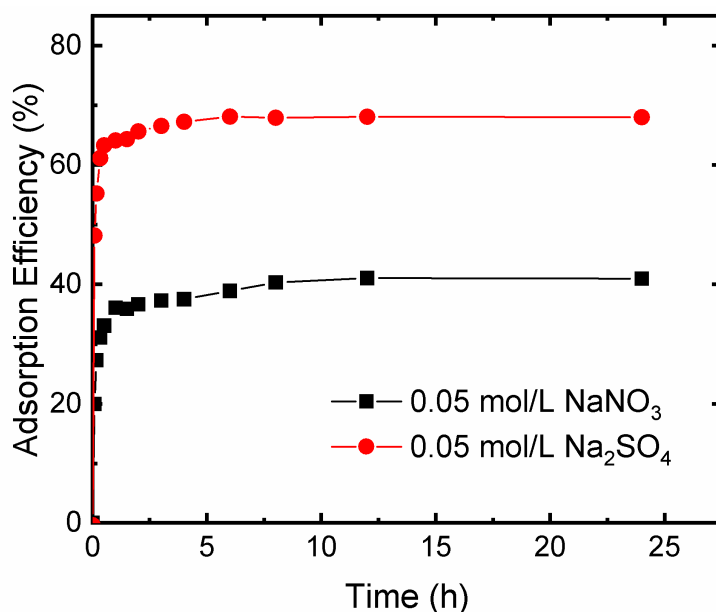


**Figure 12.** Effect of adsorption time on lanthanum adsorption by bentonite. (Initial  $\text{La}^{3+}$  concentration is 500  $\mu\text{mol/L}$ . pH is 6. Temperature is 25  $^{\circ}\text{C}$ ).

Data from the first 4 h were selected. Then, pseudo-first-order and pseudo-second-order kinetic models were used to fit the changes in adsorption capacities with time under the two electrolyte systems. The relevant results and fitting parameters are shown in Figure 13 and Table 3. By comparing the fitting correlation coefficients ( $R^2$ ), it was found that the adsorption processes of lanthanum ions by bentonite in the nitrate and sulfate systems are more consistent with the pseudo-second-order kinetic model. This is consistent

with the fact that the adsorption processes of montmorillonite on various heavy metal ions (e.g., cadmium [72] and lead [73]) conform to pseudo-second-order kinetics, indicating that both the concentration of rare earth ions and the solid–liquid ratio have impacts on the adsorption rate. The adsorption rate under the sulfate system is faster than that under the nitrate system, and the equilibrium adsorption capacity under the sulfate system is 1.75 times that of the nitrate system.

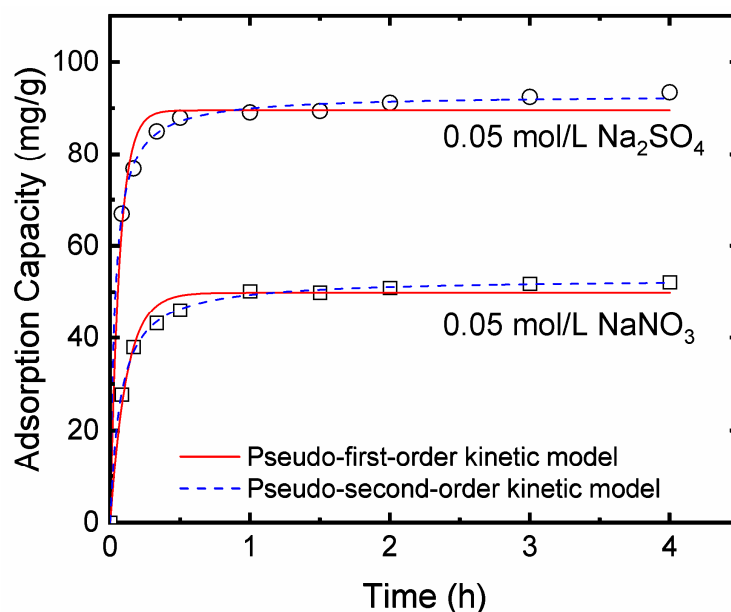


**Figure 13.** Kinetic fitting plots of lanthanum adsorption by bentonite in different background electrolytes. (Initial  $\text{La}^{3+}$  concentration is 500  $\mu\text{mol/L}$ . pH is 6. Temperature is 25  $^{\circ}\text{C}$ ).

**Table 3.** Kinetic parameters of lanthanum adsorption by bentonite in different background electrolytes.

Electrolyte	Pseudo-First-Order Kinetic Model			Pseudo-Second-Order Kinetic Model		
	$Q_e$ (mg/g)	$k_1$ (1/h)	$R^2$	$Q_e$ (mg/g)	$k_2$ (g/(mg·min))	$R^2$
$\text{NaNO}_3$	49.91	8.57	0.9813	52.99	0.26	0.9988
$\text{Na}_2\text{SO}_4$	89.57	14.82	0.9871	92.93	0.33	0.9989

### 3.4. Effect of pH

From the relationship of the suspension pH and the adsorption efficiency of lanthanum ions on the surface of bentonite (Figure 14), it can be seen that under the same background electrolyte concentration (taking 0.05 mol/L  $\text{NaNO}_3$  and  $\text{Na}_2\text{SO}_4$  as examples), whether in a sulfate system or a nitrate system, the adsorption efficiencies rise with the increase in pH (57.7% and 70.9% at pH 3 and 7 for the sulfate system; 33.9% and 49.8% at pH 3 and 7 for the nitrate system). This is consistent with the adsorption of metal ions such as  $\text{Cu}^{2+}$  and  $\text{Zn}^{2+}$  on bentonite [74]. Within the pH range of this experiment, the variation of adsorption efficiency in the nitrate (15.8%) is higher than that of sulfate (13.2%). In addition, sulfate's overall adsorption efficiency is higher than that of nitrate at the same pH.

Changes in solution pH affect not only the speciation of metal ions in the solution [75] but also the dissociation of surface functional groups [76] and the charge properties of the adsorbent surface [77]. Lanthanum mainly exists in cations in the pH range from 3.0 to 7.0. As the pH increases, the ability to neutralize the negative charges on the basal surface of the montmorillonite weakens, and the deprotonation of the edge surface elevates. The overall negative charge of the surface increases, which is beneficial to the adsorption of cations and enhances the adsorption capacity. Meanwhile, it has been established that sulfate [78] and nitrate [79] in aqueous solution can act as ligands to bridge metal ions to form complex ions.

Within the experimental pH range, besides  $\text{La}^{3+}$ , the cationic species of lanthanum in the solution may also include  $\text{LaSO}_4^+$  in the sulfate system and  $\text{LaNO}_3^{2+}$  and  $\text{La}(\text{NO}_3)_2^+$  in the nitrate system. Since  $\text{LaSO}_4^+$  has a lower positive charge than  $\text{LaNO}_3^{2+}$ , montmorillonite needs to adsorb more  $\text{LaSO}_4^+$  to neutralize the negative charge of the surface adsorption site, making the adsorption efficiency in sulfate higher than that in nitrate. Moreover,  $\text{La}(\text{NO}_3)_2^+$  with a larger molecular size is not easily accessible to the interlayer due to the steric effect, leading to a decreased adsorption capacity in the nitrate system.

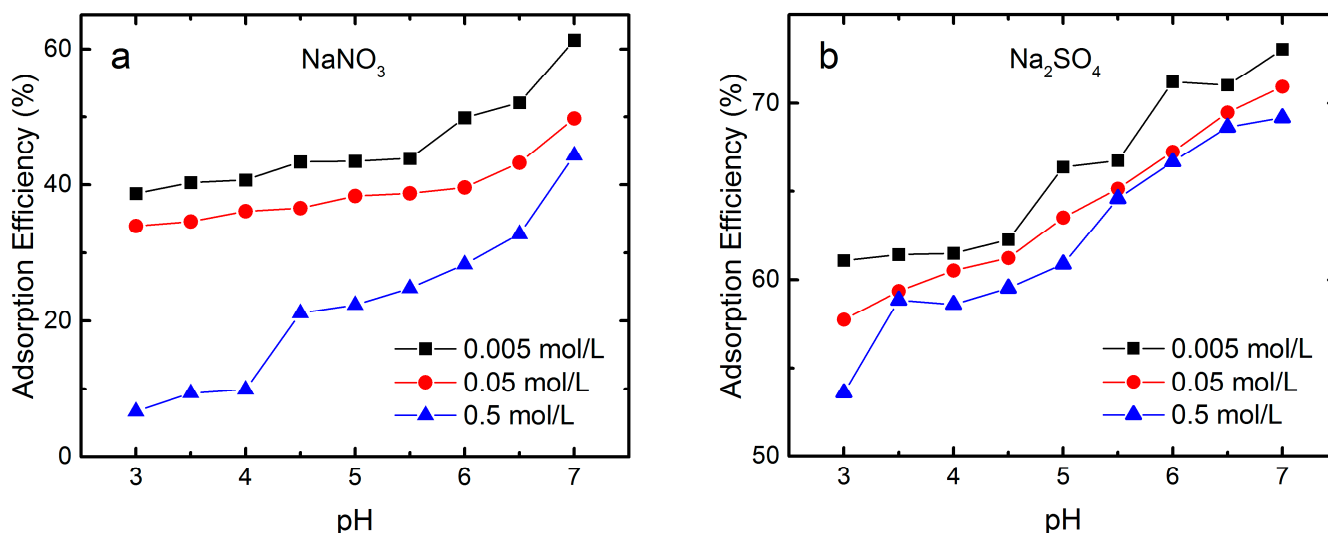


**Figure 14.** Effects of pH and background electrolyte ((a) nitrate; (b) sulfate) concentration on lanthanum adsorption by bentonite. (Initial  $\text{La}^{3+}$  concentration is 500  $\mu\text{mol/L}$ . Temperature is 25  $^{\circ}\text{C}$ . Time is 24 h).

### 3.5. Effect of Background Electrolyte Concentration

Comparing the adsorption efficiencies of lanthanum by bentonite under different sulfate and nitrate concentrations (Figure 14), it can be seen that at the same pH (taking pH 5 as an example), the adsorption efficiencies both decrease with the increased background electrolyte concentration (the sulfate concentration increases from 0.005 mol/L to 0.5 mol/L, and the adsorption efficiency decreases from 66.4% to 60.8%; the nitrate concentration increases from 0.005 mol/L to 0.5 mol/L, and the adsorption efficiency decreased from 43.4% to 22.4%). A similar phenomenon was found in the adsorption of metal cations by montmorillonite [80]. The variation of adsorption efficiency in nitrate (21.0%) is more significant than that in sulfate (5.5%). In addition, under the same ionic concentration, sulfate's overall adsorption efficiency is higher than that of nitrate.

On the one hand, the increase in background electrolyte concentration will compress the thickness of the electric double layer on the sample surface [81], reducing the electrostatic attraction between the sample surface and lanthanum ions, which is not conducive to the adsorption process. Since  $\text{LaNO}_3^{2+}$  has a higher charge than  $\text{LaSO}_4^+$ , the adsorption efficiency in nitrate is more sensitive to the changes in the background electrolyte concentration, and the variation of adsorption efficiency is more significant with the change in nitrate concentration. On the other hand, the increased background electrolyte concentration causes competitive adsorption [82] between sodium ions and lanthanum ions in the solution, thereby inhibiting the enrichment of lanthanum ions on the bentonite surface.

### 3.6. Adsorption Isotherm and Isotherm Model Fitting

The isotherms of lanthanum adsorption by bentonite in the sulfate and nitrate system at different temperatures are shown in Figure 15. All isotherms show similar characteristics: the equilibrium adsorption capacity increases rapidly at low equilibrium concentrations. Meanwhile, the higher the temperature, the faster the rate of increase in adsorption capacity.

Afterwards, the change slows down, and the isotherm gradually flattens, reaching a maximum value.

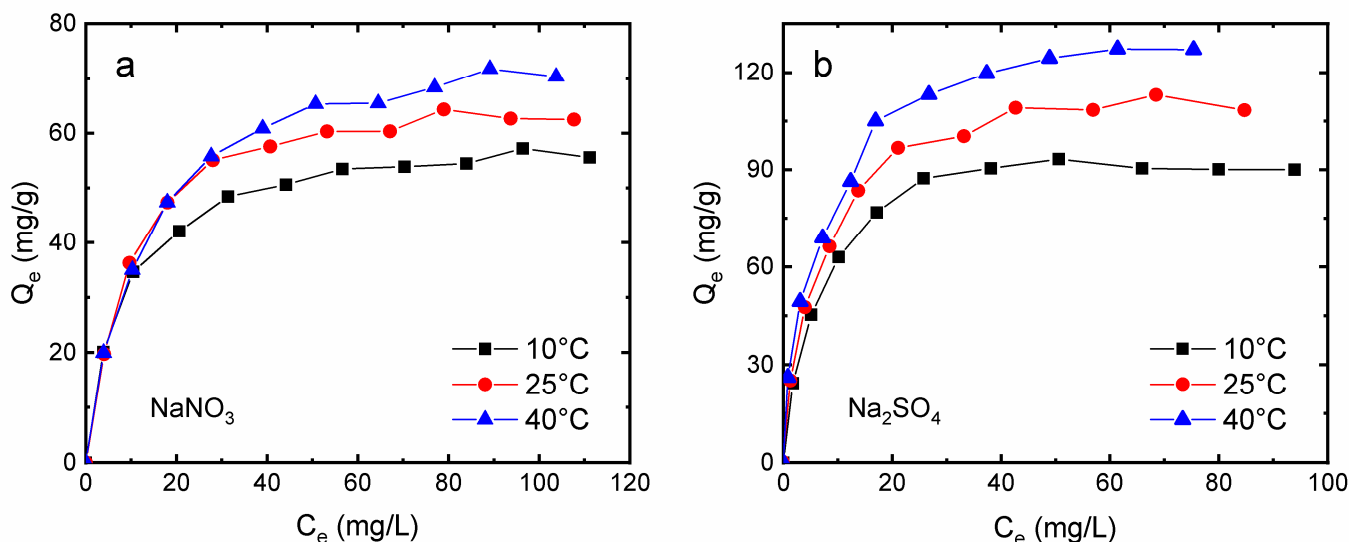


**Figure 15.** Adsorption isotherms of lanthanum by bentonite at different temperatures and background electrolytes ((a) nitrate; (b) sulfate). (Initial  $\text{La}^{3+}$  concentrations are 100, 200, 300, 400, 500, 600, 700, 800, 900, and 1000  $\mu\text{mol/L}$ . pH is 6. Background electrolyte concentration is 0.05 mol/L. Time is 24 h).

The isotherms were fitted with the Langmuir and Freundlich models (Figures 16 and 17, and Table 4). It was found that the lanthanum adsorption isotherms by bentonite in the two background electrolytes are more consistent with the Langmuir adsorption model. This is similar to the model fitting results of adsorption isotherms on montmorillonite for a variety of metal ions with different valence states (e.g., Ag(I) [83], Co(II), Fe(III) [84], Pu(IV), Pu(V) [85], and Cr(VI) [86]), indicating that it may be single-layer adsorption. The adsorption equilibrium constant ( $K_L$ ) decreases with the increase in temperature, and the maximum adsorption capacity ( $Q_{max}$ ) rises with the increase in temperature, which indicates that increasing the temperature is generally beneficial to these adsorption processes. At the same temperature, the adsorption equilibrium constant and maximum adsorption capacity of the sulfate system are higher than those of the nitrate system, indicating that the sulfate system is more conducive to the adsorption of lanthanum by bentonite.

**Table 4.** Langmuir and Freundlich model fitting parameters of lanthanum adsorption isotherms on the bentonite surface.

Electrolyte	Temperature	Langmuir Model			Freundlich Model		
	(°C)	$K_L$ (L/mg)	$Q_{max}$ (mg/g)	$R^2$	$K_F$	$n$	$R^2$
$\text{NaNO}_3$	10	0.125	60.35	0.9988	16.17	3.49	0.9047
	25	0.124	68.45	0.9980	16.01	3.10	0.8582
	40	0.083	79.55	0.9985	14.26	2.68	0.9267
$\text{Na}_2\text{SO}_4$	10	0.243	95.79	0.9985	26.42	2.92	0.9116
	25	0.188	118.34	0.9975	28.76	2.91	0.9111
	40	0.178	137.55	0.9981	32.62	2.98	0.9277

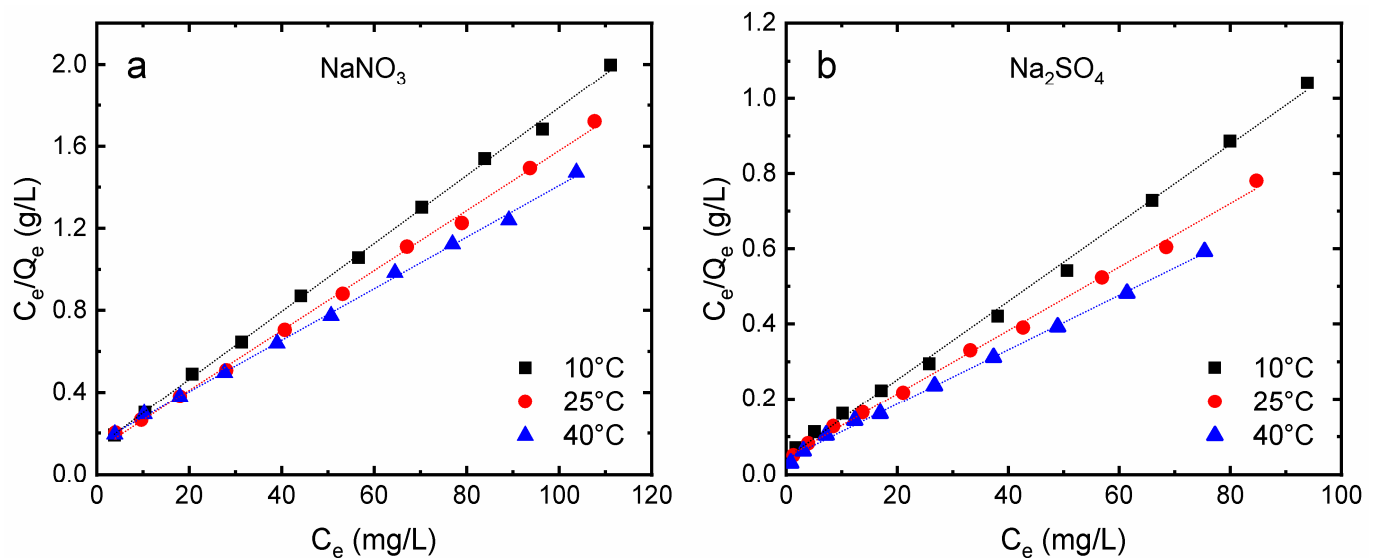


**Figure 16.** Langmuir model fitting of lanthanum adsorption isotherms on the bentonite surface in nitrate (a) and sulfate (b). (Initial La<sup>3+</sup> concentrations are 100, 200, 300, 400, 500, 600, 700, 800, 900, and 1000 µmol/L. pH is 6. Background electrolyte concentration is 0.05 mol/L. Time is 24 h).

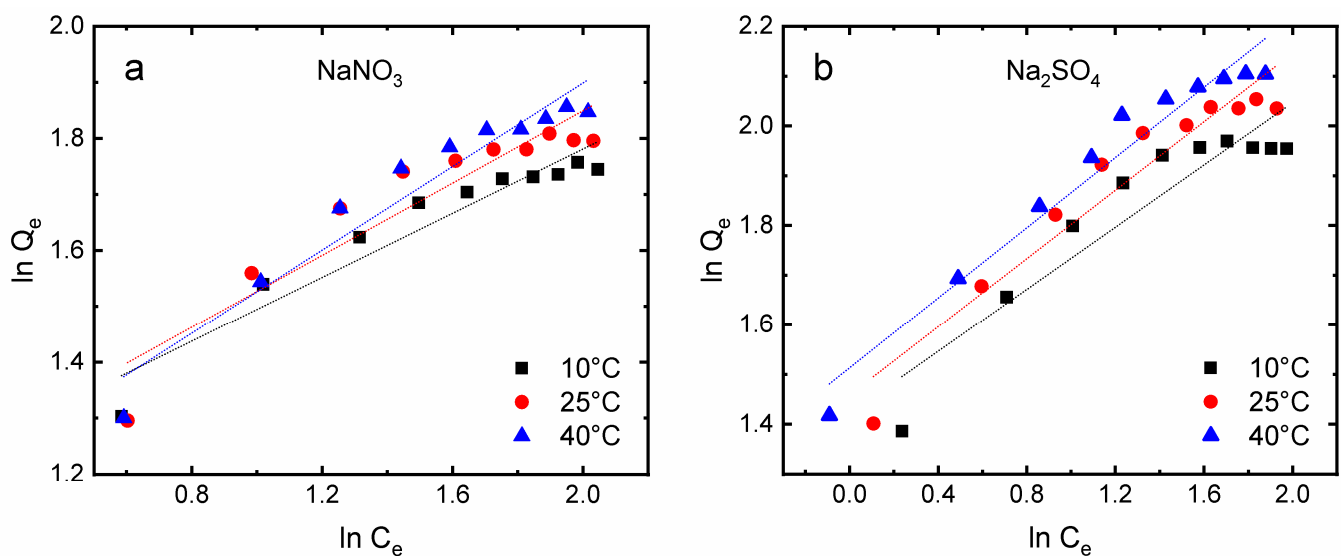


**Figure 17.** Freundlich model fitting of lanthanum adsorption isotherms on the bentonite surface in nitrate (a) and sulfate (b). (Initial La<sup>3+</sup> concentrations are 100, 200, 300, 400, 500, 600, 700, 800, 900, and 1000 µmol/L. pH is 6. Background electrolyte concentration is 0.05 mol/L. Time is 24 h).

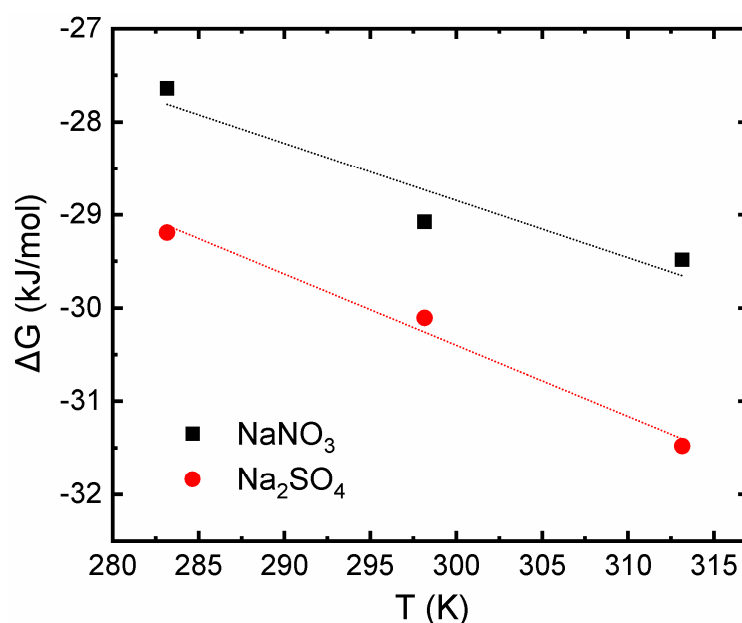
### 3.7. Adsorption Thermodynamics

Assuming that the density of the aqueous solution is 10<sup>3</sup> g/L, the unit of  $K_L$  can be transformed from L/mg to a dimensionless form. Based on the adsorption equilibrium constant ( $K_L$ ), the standard Gibbs free energy ( $\Delta G^\theta$ ) of the adsorption process can be calculated, as shown in Table 5. The standard Gibbs free energies of the adsorption processes in nitrate and sulfate at different temperatures are all negative, indicating that the adsorption of lanthanum by bentonite is a spontaneous process. The absolute values of  $\Delta G^\theta$  are all less than 40 kJ/mol. This indicates that the adsorption processes are mainly physical adsorption [87].

**Table 5.** Thermodynamic parameters of the adsorption process of lanthanum on the surface of bentonite.

Electrolyte	<i>T</i> (K)	$\Delta G^\theta$ (kJ/mol)	$\Delta H^\theta$ (kJ/mol)	$\Delta S^\theta$ (J/(mol·K))	<i>R</i> <sup>2</sup>
NaNO <sub>3</sub>	283.15	−27.64	10.38	61.54	0.9059
	298.15	−29.07			
	313.15	−29.48			
Na <sub>2</sub> SO <sub>4</sub>	283.15	−29.19	7.53	76.24	0.9866
	298.15	−30.10			
	313.15	−31.48			

Moreover,  $\Delta G^\theta$  is plotted against *T* (Figure 18). According to the intercept and slope of the fitting straight line, the standard enthalpy change ( $\Delta H^\theta$ ) and standard entropy change ( $\Delta S^\theta$ ) of the adsorption process can be determined, as shown in Table 4. The  $\Delta H^\theta$  values in the nitrate and sulfate systems are 10.38 and 7.53 kJ/mol, respectively. The positive enthalpy change value indicates that the adsorption process of lanthanum on the bentonite surface is endothermic. This is consistent with the aforementioned experimental results: the adsorption capacity increases with increasing temperature. In addition, the researchers found a similar pattern when studying the adsorption of Ni(II) and Mn(II) ions by Nigerian montmorillonite [88]. The  $\Delta S^\theta$  values in both systems are positive, indicating that the adsorption process is entropy-increasing. This is because an increased randomness occurs at the solid–solution interface [89]. The ionic radii of SO<sub>4</sub><sup>2−</sup> and NO<sub>3</sub><sup>−</sup> are 2.569 Å and 2.115 Å, respectively, which are more significant than the molecular radius of H<sub>2</sub>O (1.602 Å) [90]. Therefore, when a sulfate or nitrate is adsorbed to the surface of bentonite, more than one water molecule will desorb. Therefore, the entropy decrease caused by the adsorption of cations may be smaller than the entropy increase caused by the desorption of water molecules, resulting in the entropy change of the adsorption process having a positive value.

**Figure 18.** Van't Hoff plots of lanthanum adsorption on bentonite.

### 3.8. Adsorption Mechanism

The main component of the bentonite used in this experiment is montmorillonite. Montmorillonite possesses two types of surfaces: the basal surface with permanent negative charges and the edge surface with variable charges [50]. According to the results of potentiometric titration, the point of zero charge of the edge surface is 9.5, so the edge

surface is positively charged within the pH range from 3 to 7 used in this experiment, which is not conducive to the adsorption of rare earth cations. It can be inferred that rare earth ions are mainly adsorbed on the basal surface between montmorillonite layers through ion exchange, a general mechanism for metal ion adsorption and enrichment on montmorillonite [91]. This also agrees with the mechanism obtained by Coppin et al. [45] concerning the adsorption of the entire lanthanide series on clay minerals, where the adsorption coefficient is closely related to the cation exchange capacity. At the same time, in the sulfate and nitrate solution systems, sulfate and nitrate can act as ligands to bind metal ions ( $\text{La}^{3+}$ ) to form complex cations [78,79], such as  $\text{LaSO}_4^+$ ,  $\text{LaNO}_3^{2+}$ , and  $\text{La}(\text{NO}_3)_2^+$ . Since  $\text{LaSO}_4^+$  has a lower positive charge than  $\text{LaNO}_3^{2+}$ , more  $\text{LaSO}_4^+$  is needed to exchange the same amount of montmorillonite interlayer cations compared with  $\text{LaNO}_3^{2+}$ . This is why the adsorption capacity of lanthanum by bentonite in the sulfate system is higher than that of the nitrate system. This is consistent with the previous study: at  $\text{pH} < 7$ , montmorillonite adsorbs more monovalent cations ( $\text{Ag}^+$ ) than divalent cations ( $\text{Cu}^{2+}$ ) [83]. Meanwhile, the more significant steric hindrance of  $\text{La}(\text{NO}_3)_2^+$  will limit its exchange behavior with interlayer cations due to its larger molecular size, contributing to the lower adsorption of rare earth ions in the nitrate system than in the sulfate system. Moreover, a few tiny amorphous mineral particles and organic matter generally contained in the bentonite may also contribute to adsorption.

#### 4. Conclusions

Bentonite is a cheap and efficient natural adsorbent widely used for removing heavy metal ions, including rare earth elements. However, there needs to be more research on the adsorption behavior and mechanism of rare earth ions on bentonite under a sulfate system. This paper compared the adsorption behavior of lanthanum ions by bentonite in sulfate and nitrate systems by exploring the effects of adsorption time, pH, background electrolyte concentration, and initial rare earth ion concentration. It was found that the adsorption processes in both systems include two steps: a rapid adsorption step and a slow equilibrium step. The adsorption kinetic processes are more consistent with the pseudo-second-order kinetic model, and the adsorption rate of the sulfate system is higher than that of the nitrate system. The adsorption efficiencies of lanthanum cations in the two systems rise with the increase in pH and the decrease in background electrolyte concentration, and the adsorption efficiency in the nitrate system is more sensitive to changes in pH and background electrolyte concentration. Under the same pH and ionic concentration, the overall adsorption efficiency in the sulfate system is higher than that in the nitrate system. The isotherms of lanthanum adsorption by bentonite in the two background electrolytes are more consistent with the Langmuir adsorption model. The adsorption processes are both spontaneous physical adsorption, endothermic, and entropy-increasing processes. The adsorption capacity of lanthanum by bentonite in the sulfate system is higher than that in the nitrate system, presumably because  $\text{LaSO}_4^+$  has a lower positive charge than  $\text{LaNO}_3^{2+}$ , so more  $\text{LaSO}_4^+$  is needed to exchange the same amount of interlayer cations. This study contributes to understanding the adsorption behavior and mechanism of rare earth ions on bentonite under a sulfate system. It provides information on removing and recovering rare earth elements from mine drainage.

**Author Contributions:** Conceptualization, Z.Q., W.Y., X.N. and Q.W.; methodology, Z.Q. and Z.Z.; investigation, Z.Q. and Z.Z.; resources, Z.Q. and Q.W.; funding acquisition, Z.Q. and Q.W.; data curation, Z.Q. and Z.Z.; project administration, S.Y. (Shuguang Yang) and S.Y. (Shuqin Yang); writing—original draft preparation, Z.Q. and Z.Z.; writing—review and editing, Z.Q. and Q.W.; visualization, Z.Q.; supervision, Z.Q. and Q.W. All authors have read and agreed to the published version of the manuscript.

**Funding:** This work was financially supported by the National Natural Science Foundation of China (41872046), the B-type Strategic Priority Program of the Chinese Academy of Sciences (XDB41000000), the Guizhou Provincial Basic Research Program (Natural Science) ([2019]1460), and the Frontier Program of State Key Laboratory of Ore Deposit Geochemistry (SKLODG-2018-01).

**Data Availability Statement:** Data will be made available on request.

**Conflicts of Interest:** The authors declare that they have no known competing financial interests or personal relationships that could have appeared to influence the work reported in this paper.

## References

1. Cheisson, T.; Schelter, E.J. Rare earth elements: Mendeleev's bane, modern marvels. *Science* **2019**, *363*, 489–493. [\[CrossRef\]](#) [\[PubMed\]](#)
2. Imandoust, A.; Barrett, C.D.; Al-Samman, T.; Inal, K.A.; El Kadiri, H. A review on the effect of rare-earth elements on texture evolution during processing of magnesium alloys. *J. Mater. Sci.* **2017**, *52*, 1–29. [\[CrossRef\]](#)
3. Lyubov, D.M.; Tolpygin, A.O.; Trifonov, A.A. Rare-earth metal complexes as catalysts for ring-opening polymerization of cyclic esters. *Coord. Chem. Rev.* **2019**, *392*, 83–145. [\[CrossRef\]](#)
4. Oses, C.; Toher, C.; Curtarolo, S. High-entropy ceramics. *Nat. Rev. Mater.* **2020**, *5*, 295–309. [\[CrossRef\]](#)
5. Coey, J.M.D. Perspective and Prospects for Rare Earth Permanent Magnets. *Engineering* **2020**, *6*, 119–131. [\[CrossRef\]](#)
6. Foltyn, S.R.; Civale, L.; Macmanus-Driscoll, J.L.; Jia, Q.X.; Maiorov, B.; Wang, H.; Maley, M. Materials science challenges for high-temperature superconducting wire. *Nat. Mater.* **2007**, *6*, 631–642. [\[CrossRef\]](#)
7. Srikant; Sharma, V.K.; Kumar, V.; Joshi, R.S.; Jain, S.; Kumar, P. A Review of Recent Research on Rare Earth Particulate Composite Materials and Structures with Their Applications. *Trans. Indian Inst. Met.* **2021**, *74*, 2569–2581. [\[CrossRef\]](#)
8. Gulley, A.L.; Nassar, N.T.; Xun, S. China, the United States, and competition for resources that enable emerging technologies. *PNAS* **2018**, *115*, 4111–4115. [\[CrossRef\]](#)
9. Balaram, V. Rare earth elements: A review of applications, occurrence, exploration, analysis, recycling, and environmental impact. *Geosci. Front.* **2019**, *10*, 1285–1303. [\[CrossRef\]](#)
10. Balaram, V. Potential Future Alternative Resources for Rare Earth Elements: Opportunities and Challenges. *Minerals* **2023**, *13*, 425. [\[CrossRef\]](#)
11. Binnemans, K.; Jones, P.T.; Blanpain, B.; Van Gerven, T.; Pontikes, Y. Towards zero-waste valorisation of rare-earth-containing industrial process residues: A critical review. *J. Clean. Prod.* **2015**, *99*, 17–38. [\[CrossRef\]](#)
12. Pyrgaki, K.; Gemeni, V.; Karkalis, C.; Koukouzas, N.; Koutsovitis, P.; Petrounias, P. Geochemical Occurrence of Rare Earth Elements in Mining Waste and Mine Water: A Review. *Minerals* **2021**, *11*, 860. [\[CrossRef\]](#)
13. Royer-Lavallée, A.; Neculita, C.M.; Coudert, L. Removal and potential recovery of rare earth elements from mine water. *J. Ind. Eng. Chem.* **2020**, *89*, 47–57. [\[CrossRef\]](#)
14. Benalia, M.C.; Youcef, L.; Bouaziz, M.G.; Achour, S.; Menasra, H. Removal of Heavy Metals from Industrial Wastewater by Chemical Precipitation: Mechanisms and Sludge Characterization. *Arab. J. Sci. Eng.* **2022**, *47*, 5587–5599. [\[CrossRef\]](#)
15. Taseidifar, M.; Makavipour, F.; Pashley, R.M.; Rahman, A.F.M.M. Removal of heavy metal ions from water using ion flotation. *Environ. Technol. Innov.* **2017**, *8*, 182–190. [\[CrossRef\]](#)
16. Hossain, M.S.; Omar, F.; Asis, A.J.; Bachmann, R.T.; Islam Sarker, M.Z.; Ab Kadir, M.O. Effective treatment of palm oil mill effluent using FeSO<sub>4</sub>·7H<sub>2</sub>O waste from titanium oxide industry: Coagulation adsorption isotherm and kinetics studies. *J. Clean. Prod.* **2019**, *219*, 86–98. [\[CrossRef\]](#)
17. Xiao, X.; Sun, Y.; Liu, J.; Zheng, H. Flocculation of heavy metal by functionalized starch-based bioflocculants: Characterization and process evaluation. *Sep. Purif. Technol.* **2021**, *267*, 118628. [\[CrossRef\]](#)
18. Nafti-Mateur, M.; Jaouadi, M.; Van der Bruggen, B.; Naifer, K.H.; Jellouli Ennigrou, D. Development and characterization of porous membranes based on PPSU/PES using polyethylene glycol as porogen: Application for cobalt removal by polyelectrolyte-enhanced ultrafiltration. *J. Chem. Technol. Biotechnol.* **2024**, *99*, 343–354. [\[CrossRef\]](#)
19. Samavati, Z.; Samavati, A.; Goh, P.S.; Fauzi Ismail, A.; Sohaimi Abdullah, M. A comprehensive review of recent advances in nanofiltration membranes for heavy metal removal from wastewater. *Chem. Eng. Res. Des.* **2023**, *189*, 530–571. [\[CrossRef\]](#)
20. Graillot, A.; Cojocariu, C.; Bouyer, D.; Monge, S.; Mauchauffe, S.; Robin, J.-J.; Faur, C. Thermosensitive polymer Enhanced Filtration (TEF) process: An innovative process for heavy metals removal and recovery from industrial wastewaters. *Sep. Purif. Technol.* **2015**, *141*, 17–24. [\[CrossRef\]](#)
21. Sagar Jena, P.; Pradhan, A.; Prakash Nanda, S.; Kishore Dash, A.; Naik, B. Biosorption of heavy metals from wastewater using *Saccharomyces cerevisiae* as a biosorbent: A mini review. *Mater. Today Proc.* **2022**, *67*, 1140–1146. [\[CrossRef\]](#)
22. Arana Juve, J.-M.; Christensen, F.M.S.; Wang, Y.; Wei, Z. Electrodialysis for metal removal and recovery: A review. *Chem. Eng. J.* **2022**, *435*, 134857. [\[CrossRef\]](#)
23. Chen, L.; Wang, X.; Chen, Y.; Zhuang, Z.; Chen, F.-F.; Zhu, Y.-J.; Yu, Y. Recycling heavy metals from wastewater for photocatalytic CO<sub>2</sub> reduction. *Chem. Eng. J.* **2020**, *402*, 125922. [\[CrossRef\]](#)
24. Binnemans, K.; Jones, P.T.; Blanpain, B.; Van Gerven, T.; Yang, Y.X.; Walton, A.; Buchert, M. Recycling of rare earths: A critical review. *J. Clean. Prod.* **2013**, *51*, 1–22. [\[CrossRef\]](#)
25. Negrea, A.; Gabor, A.; Davidescu, C.M.; Ciopec, M.; Negrea, P.; Duteanu, N.; Barbulescu, A. Rare Earth Elements Removal from Water Using Natural Polymers. *Sci. Rep.* **2018**, *8*, 316. [\[CrossRef\]](#)
26. Cao, Y.; Shao, P.; Chen, Y.; Zhou, X.; Yang, L.; Shi, H.; Yu, K.; Luo, X.; Luo, X. A critical review of the recovery of rare earth elements from wastewater by algae for resources recycling technologies. *Resour. Conserv. Recycl.* **2021**, *169*, 105519. [\[CrossRef\]](#)

27. Hu, K.; Liu, Y.; Zhou, X.; Hussain, S.; Li, K.; Chen, Q.; Zhang, C.; Song, W.; Li, X.; Wan, Y. Highly selective recovery of rare earth elements from mine wastewater by modifying kaolin with phosphoric acid. *Sep. Purif. Technol.* **2023**, *309*, 123117. [\[CrossRef\]](#)
28. Awual, M.R.; Hasan, M.N.; Hasan, M.M.; Salman, M.S.; Sheikh, M.C.; Kubra, K.T.; Islam, M.S.; Marwani, H.M.; Islam, A.; Khaleque, M.A.; et al. Green and robust adsorption and recovery of Europium(III) with a mechanism using hybrid donor conjugate materials. *Sep. Purif. Technol.* **2023**, *319*, 124088. [\[CrossRef\]](#)
29. Kegl, T.; Kosak, A.; Lobnik, A.; Novak, Z.; Kralj, A.K.; Ban, I. Adsorption of rare earth metals from wastewater by nanomaterials: A review. *J. Hazard. Mater.* **2020**, *386*, 121632. [\[CrossRef\]](#)
30. Gładysz-Plaska, A.; Majdan, M.; Pikus, S. Adsorption of lanthanides on mordenite from nitrate medium. *J. Colloid Interface Sci.* **2008**, *317*, 409–423. [\[CrossRef\]](#)
31. Kubra, K.T.; Hasan, M.M.; Hasan, M.N.; Salman, M.S.; Khaleque, M.A.; Sheikh, M.C.; Rehan, A.I.; Rasee, A.I.; Waliullah, R.M.; Awual, M.E.; et al. The heavy lanthanide of Thulium(III) separation and recovery using specific ligand-based facial composite adsorbent. *Colloids Surf. A* **2023**, *667*, 131415. [\[CrossRef\]](#)
32. Kolodynska, D.; Krukowska, J.; Thomas, P. Comparison of sorption and desorption studies of heavy metal ions from biochar and commercial active carbon. *Chem. Eng. J.* **2017**, *307*, 353–363. [\[CrossRef\]](#)
33. Erdem, E.; Karapinar, N.; Donat, R. The removal of heavy metal cations by natural zeolites. *J. Colloid Interface Sci.* **2004**, *280*, 309–314. [\[CrossRef\]](#)
34. Lin, S.H.; Lai, S.L.; Leu, H.G. Removal of heavy metals from aqueous solution by chelating resin in a multistage adsorption process. *J. Hazard. Mater.* **2000**, *76*, 139–153. [\[CrossRef\]](#)
35. Eissa, M.E.; Sakr, A.K.; Hanfi, M.Y.; Sayyed, M.I.; Al-Otaibi, J.S.; Abdel-lateef, A.M.; Cheira, M.F.; Abdelmonem, H.A. Physico-chemical investigation of mercury sorption on mesoporous thioacetamide/chitosan from wastewater. *Chemosphere* **2023**, *341*, 140062. [\[CrossRef\]](#)
36. Abdelmonem, H.A.; Hassanein, T.F.; Sharafeldin, H.E.; Gomaa, H.; Ahmed, A.S.A.; Abdel-lateef, A.M.; Allam, E.M.; Cheira, M.F.; Eissa, M.E.; Tilp, A.H. Cellulose-embedded polyacrylonitrile/amidoxime for the removal of cadmium (II) from wastewater: Adsorption performance and proposed mechanism. *Colloids Surf. A* **2024**, *684*, 133081. [\[CrossRef\]](#)
37. Novikau, R.; Lujanienė, G. Adsorption behaviour of pollutants: Heavy metals, radionuclides, organic pollutants, on clays and their minerals (raw, modified and treated): A review. *J. Environ. Manag.* **2022**, *309*, 114685. [\[CrossRef\]](#)
38. Gomaa, H.; Shenashen, M.A.; Elbaz, A.; Kawada, S.; Seaf El-Nasr, T.A.; Cheira, M.F.; Eid, A.I.; El-Safty, S.A. Inorganic-organic mesoporous hybrid segregators for selective and sensitive extraction of precious elements from urban mining. *J. Colloid Interface Sci.* **2021**, *604*, 61–79. [\[CrossRef\]](#) [\[PubMed\]](#)
39. Brigatti, M.F.; Galán, E.; Theng, B.K.G. Structure and mineralogy of clay minerals. In *Handbook of Clay Science*, 2nd ed.; Bergaya, F., Lagaly, G., Eds.; Developments in Clay Science; Elsevier: Amsterdam, The Netherlands, 2013; pp. 21–81.
40. Schoonheydt, R.A.; Johnston, C.T.; Bergaya, F. Clay minerals and their surfaces. In *Surface and Interface Chemistry of Clay Minerals*; Schoonheydt, R., Johnston, C.T., Bergaya, F., Eds.; Developments in Clay Science; Elsevier: Amsterdam, The Netherlands, 2018; pp. 1–21.
41. Bhattacharyya, K.G.; Sen Gupta, S. Adsorption of a few heavy metals on natural and modified kaolinite and montmorillonite: A review. *Adv. Colloid Interface Sci.* **2008**, *140*, 114–131. [\[CrossRef\]](#) [\[PubMed\]](#)
42. Al Kausor, M.; Sen Gupta, S.; Bhattacharyya, K.G.; Chakraborty, D. Montmorillonite and modified montmorillonite as adsorbents for removal of water soluble organic dyes: A review on current status of the art. *Inorg. Chem. Commun.* **2022**, *143*, 109686. [\[CrossRef\]](#)
43. Zhang, B.; Gao, B.; Ma, W.J.; Wang, S.Q.; Qi, W.B.; Wu, J.Z.; Wang, R.; Zhou, Y.J.; Liu, Y.Y. Different behavior of uranium(VI) on two clay minerals: Montmorillonite and kaolinite. *J. Radioanal. Nucl. Chem.* **2023**, *332*, 4029–4046. [\[CrossRef\]](#)
44. Cheira, M.F.; Rashed, M.N.; Mohamed, A.E.; Zidan, I.H.; Awadallah, M.A. The performance of Alizarin impregnated bentonite for the displacement of some heavy metals ions from the wet phosphoric acid. *Sep. Sci. Technol.* **2020**, *55*, 3072–3088. [\[CrossRef\]](#)
45. Coppin, F.; Berger, G.; Bauer, A.; Castet, S.; Loubet, M. Sorption of lanthanides on smectite and kaolinite. *Chem. Geol.* **2002**, *182*, 57–68. [\[CrossRef\]](#)
46. Alshameri, A.; Hongping, H.; Chen, X.; Jianxi, Z.; Wei, X.H.; Runliang, Z.; Hailong, W. Understanding the role of natural clay minerals as effective adsorbents and alternative source of rare earth elements: Adsorption operative parameters. *Hydrometallurgy* **2019**, *185*, 149–161. [\[CrossRef\]](#)
47. Fang, Z.; Suhua, H.; Xu, L.; Jian, F.; Qi, L.; Zhiwei, W.; Chuanchang, L.; Yuanlai, X. Adsorption kinetics and thermodynamics of rare earth on Montmorillonite modified by sulfuric acid. *Colloids Surf. A* **2021**, *627*, 127063. [\[CrossRef\]](#)
48. Wang, J. Adsorption of aqueous neodymium, europium, gadolinium, terbium, and yttrium ions onto nZVI-montmorillonite: Kinetics, thermodynamic mechanism, and the influence of coexisting ions. *Environ. Sci. Pollut. Res.* **2018**, *25*, 33521–33537. [\[CrossRef\]](#)
49. Sadri, F.; Nazari, A.M.; Ghahreman, A. A review on the cracking, baking and leaching processes of rare earth element concentrates. *J. Rare Earths* **2017**, *35*, 739–752. [\[CrossRef\]](#)
50. Wang, H.; Wang, X.; Wang, Y.; Wang, D.; Hu, K.; Zhong, W.; Guo, Z. Influence of ammonium sulfate leaching agent on engineering properties of weathered crust elution-deposited rare earth ore. *Acta Geotech.* **2023**, 1–22. [\[CrossRef\]](#)
51. Costis, S.; Mueller, K.K.; Coudert, L.; Neculita, C.M.; Reynier, N.; Blais, J.-F. Recovery potential of rare earth elements from mining and industrial residues: A review and cases studies. *J. Geochem. Explor.* **2021**, *221*, 106699. [\[CrossRef\]](#)

52. Tian, P.; Yang, X.; Yuan, W. Formation and preservation of the Bayan Obo Fe-REE-Nb deposit, Inner Mongolia: Insights from evidences of petrogenesis, geochemistry and apatite fission track dating. *Solid Earth Sci.* **2021**, *6*, 228–245. [[CrossRef](#)]
53. Cheira, M.F. Performance of poly sulfonamide/nano-silica composite for adsorption of thorium ions from sulfate solution. *SN Appl. Sci.* **2020**, *2*, 398. [[CrossRef](#)]
54. Liu, Q.; Li, X.; Zeng, L.; Guo, C.; Dang, Z. Effect of Sulfate on Cu(II) Adsorption/Desorption Behavior on Ferrihydrite Colloids and Cu Speciation. *ACS Earth Space Chem.* **2023**, *7*, 1496–1504. [[CrossRef](#)]
55. Gu, Q.; Liu, J.; Yang, Y.; Zhu, R.; Ma, L.; Liang, X.; Long, S.; Zhu, J.; He, H. The different effects of sulfate on the adsorption of REEs on kaolinite and ferrihydrite. *Appl. Clay Sci.* **2022**, *221*, 106468. [[CrossRef](#)]
56. Gillman, G.P.; Bruce, R.C.; Davey, B.G.; Kimble, J.M.; Searle, P.L.; Skjemstad, J.O. A comparison of methods used for determination of cation-exchange capacity. *Commun. Soil Sci. Plant Anal.* **1983**, *14*, 1005–1014. [[CrossRef](#)]
57. Brunauer, S.; Emmett, P.H.; Teller, E. Adsorption of Gases in Multimolecular Layers. *J. Am. Chem. Soc.* **1938**, *60*, 309–319. [[CrossRef](#)]
58. Olivier, J.P.; Conklin, W.B.; Szombathely, M.v. Determination of Pore Size Distribution from Density Functional Theory: A Comparison of Nitrogen and Argon Results. In *Studies in Surface Science and Catalysis*; Rouquerol, J., Rodríguez-Reinoso, F., Sing, K.S.W., Unger, K.K., Eds.; Elsevier: Amsterdam, The Netherlands, 1994; Volume 87, pp. 81–89.
59. Savvin, S.B. Analytical use of arsenazo III: Determination of thorium, zirconium, uranium and rare earth elements. *Talanta* **1961**, *8*, 673–685. [[CrossRef](#)]
60. Guo, X.M.; Yan, Q.C.; Meng, X.T.; Ma, R.X. UV-Visible Spectrophotometry with Arsenazo III for the Determination of Samarium. *J. Appl. Spectrosc.* **2019**, *86*, 542–548. [[CrossRef](#)]
61. Saleh, T.A. Kinetic models and thermodynamics of adsorption processes: Classification. In *Interface Science and Technology*; Saleh, T.A., Ed.; Elsevier: Amsterdam, The Netherlands, 2022; Volume 34, pp. 65–97.
62. Wang, J.; Guo, X. Adsorption isotherm models: Classification, physical meaning, application and solving method. *Chemosphere* **2020**, *258*, 127279. [[CrossRef](#)] [[PubMed](#)]
63. Tran, H.N.; Lima, E.C.; Juang, R.-S.; Bollinger, J.-C.; Chao, H.-P. Thermodynamic parameters of liquid-phase adsorption process calculated from different equilibrium constants related to adsorption isotherms: A comparison study. *J. Environ. Chem. Eng.* **2021**, *9*, 106674. [[CrossRef](#)]
64. Bish, D.L.; Duffy, C.J. Thermogravimetric Analysis of Minerals. In *Thermal Analysis in Clay Science*; Clay Minerals Society: Chantilly, VA, USA, 1990; Volume 3, pp. 96–192.
65. Thommes, M.; Kaneko, K.; Neimark, A.V.; Olivier, J.P.; Rodríguez-Reinoso, F.; Rouquerol, J.; Sing, K.S.W. Physisorption of gases, with special reference to the evaluation of surface area and pore size distribution (IUPAC Technical Report). *Pure Appl. Chem.* **2015**, *87*, 1051–1069. [[CrossRef](#)]
66. Schoonheydt, R.A.; Johnston, C.T. Surface and interface chemistry of clay minerals. In *Handbook of Clay Science*, 2nd ed.; Bergaya, F., Lagaly, G., Eds.; Developments in Clay Science; Elsevier: Amsterdam, The Netherlands, 2013; pp. 139–172.
67. Kraepiel, A.M.L.; Keller, K.; Morel, F.M.M. On the acid-base chemistry of permanently charged minerals. *Environ. Sci. Technol.* **1998**, *32*, 2829–2838. [[CrossRef](#)]
68. Barhoum, A.; Garcia-Betancourt, M.L.; Rahier, H.; Van Assche, G. Physicochemical characterization of nanomaterials: Polymorph, composition, wettability, and thermal stability. In *Emerging Applications of Nanoparticles and Architecture Nanostructures*; Barhoum, A., Makhoul, A.S.H., Eds.; Elsevier: Amsterdam, The Netherlands, 2018; pp. 255–278.
69. Madejová, J. FTIR techniques in clay mineral studies. *Vib. Spectrosc.* **2003**, *31*, 1–10. [[CrossRef](#)]
70. Ahmed, A.; Chaker, Y.; Belarbi, E.H.; Abbas, O.; Chotard, J.N.; Abassi, H.B.; Van Nhien, A.N.; El Hadri, M.; Bresson, S. XRD and ATR/FTIR investigations of various montmorillonite clays modified by monocationic and dicationic imidazolium ionic liquids. *J. Mol. Struct.* **2018**, *1173*, 653–664. [[CrossRef](#)]
71. Ghorbel-Abid, I.; Jrad, A.; Nahdi, K.; Trabelsi-Ayadi, M. Sorption of chromium (III) from aqueous solution using bentonitic clay. *Desalination* **2009**, *246*, 595–604. [[CrossRef](#)]
72. Yan, L.; Shan, X.; Wen, B.; Owens, G. Adsorption of cadmium onto Al<sub>13</sub>-pillared acid-activated montmorillonite. *J. Hazard. Mater.* **2008**, *156*, 499–508. [[CrossRef](#)] [[PubMed](#)]
73. Zhang, S.Q.; Hou, W.G. Adsorption behavior of Pb(II) on montmorillonite. *Colloids Surf. A* **2008**, *320*, 92–97. [[CrossRef](#)]
74. Veli, S.; Alyüz, B. Adsorption of copper and zinc from aqueous solutions by using natural clay. *J. Hazard. Mater.* **2007**, *149*, 226–233. [[CrossRef](#)]
75. Huang, J.; Yuan, F.; Zeng, G.; Li, X.; Gu, Y.; Shi, L.; Liu, W.; Shi, Y. Influence of pH on heavy metal speciation and removal from wastewater using micellar-enhanced ultrafiltration. *Chemosphere* **2017**, *173*, 199–206. [[CrossRef](#)] [[PubMed](#)]
76. Jeon, I.; Nam, K. Change in the site density and surface acidity of clay minerals by acid or alkali spills and its effect on pH buffering capacity. *Sci. Rep.* **2019**, *9*, 9878. [[CrossRef](#)]
77. Tombácz, E.; Szekeres, M. Surface charge heterogeneity of kaolinite in aqueous suspension in comparison with montmorillonite. *Appl. Clay Sci.* **2006**, *34*, 105–124. [[CrossRef](#)]
78. Papatriantafyllopoulou, C.; Manessi-Zoupa, E.; Escuer, A.; Perlepes, S.P. The sulfate ligand as a promising “player” in 3d-metal cluster chemistry. *Inorg. Chim. Acta* **2009**, *362*, 634–650. [[CrossRef](#)]
79. Addison, C.C.; Sutton, D. Complexes Containing the Nitrate Ion. In *Progress in Inorganic Chemistry*; John Wiley & Sons, Inc.: Hoboken, NJ, USA, 1967; pp. 195–286.

80. Xu, D.; Zhou, X.; Wang, X. Adsorption and desorption of  $\text{Ni}^{2+}$  on Na-montmorillonite: Effect of pH, ionic strength, fulvic acid, humic acid and addition sequences. *Appl. Clay Sci.* **2008**, *39*, 133–141. [[CrossRef](#)]
81. Tombácz, E.; Szekeres, M. Colloidal behavior of aqueous montmorillonite suspensions: The specific role of pH in the presence of indifferent electrolytes. *Appl. Clay Sci.* **2004**, *27*, 75–94. [[CrossRef](#)]
82. Orucoglu, E.; Grangeon, S.; Gloter, A.; Robinet, J.C.; Madé, B.; Tournassat, C. Competitive Adsorption Processes at Clay Mineral Surfaces: A Coupled Experimental and Modeling Approach. *ACS Earth Space Chem.* **2022**, *6*, 144–159. [[CrossRef](#)]
83. Alandis, N.M.; Mekhamer, W.; Aldayel, O.; Hefne, J.A.A.; Alam, M. Adsorptive Applications of Montmorillonite Clay for the Removal of Ag(I) and Cu(II) from Aqueous Medium. *J. Chem.* **2019**, *2019*, 7129014. [[CrossRef](#)]
84. Bhattacharyya, K.G.; Gupta, S.S. Kaolinite and montmorillonite as adsorbents for Fe(III), Co(II) and Ni(II) in aqueous medium. *Appl. Clay Sci.* **2008**, *41*, 1–9. [[CrossRef](#)]
85. Begg, J.D.; Zavarin, M.; Zhao, P.; Tumey, S.J.; Powell, B.; Kersting, A.B. Pu(V) and Pu(IV) Sorption to Montmorillonite. *Environ. Sci. Technol.* **2013**, *47*, 5146–5153. [[CrossRef](#)] [[PubMed](#)]
86. Wang, G.; Hua, Y.; Su, X.; Komarneni, S.; Ma, S.; Wang, Y. Cr(VI) adsorption by montmorillonite nanocomposites. *Appl. Clay Sci.* **2016**, *124–125*, 111–118. [[CrossRef](#)]
87. Wei, M.; Marrakchi, F.; Yuan, C.; Cheng, X.; Jiang, D.; Zafar, F.F.; Fu, Y.; Wang, S. Adsorption modeling, thermodynamics, and DFT simulation of tetracycline onto mesoporous and high-surface-area NaOH-activated macroalgae carbon. *J. Hazard. Mater.* **2022**, *425*, 127887. [[CrossRef](#)] [[PubMed](#)]
88. Akpomie, K.G.; Dawodu, F.A.; Adebawale, K.O. Mechanism on the sorption of heavy metals from binary-solution by a low cost montmorillonite and its desorption potential. *Alex. Eng. J.* **2015**, *54*, 757–767. [[CrossRef](#)]
89. Ho, Y.S. Removal of copper ions from aqueous solution by tree fern. *Water Res.* **2003**, *37*, 2323–2330. [[CrossRef](#)] [[PubMed](#)]
90. Mantina, M.; Chamberlin, A.C.; Valero, R.; Cramer, C.J.; Truhlar, D.G. Consistent van der Waals Radii for the Whole Main Group. *J. Phys. Chem. A* **2009**, *113*, 5806–5812. [[CrossRef](#)] [[PubMed](#)]
91. Bergaya, F.; Lagaly, G.; Vayer, M. Cation and Anion Exchange. In *Developments in Clay Science*; Bergaya, F., Lagaly, G., Eds.; Elsevier: Amsterdam, The Netherlands, 2013; Volume 5, pp. 333–359.

**Disclaimer/Publisher’s Note:** The statements, opinions and data contained in all publications are solely those of the individual author(s) and contributor(s) and not of MDPI and/or the editor(s). MDPI and/or the editor(s) disclaim responsibility for any injury to people or property resulting from any ideas, methods, instructions or products referred to in the content.